DOI 10.1007/s10812-023-01627-2
Journal of Applied Spectroscopy, Vol. 90, No. 5, November, 2023 (Russian Original Vol. 90, No. 5, September–October, 2023)

SPECTRAL AND NEAR-FIELD SCATTERING CHARACTERISTICS OF TWO-LAYERED METAL-CONTAINING NANOPARTICLES IN ABSORBING MATRICES

R. A. Dynich* **and A. N. Ponyavina**

UDC 53.343

The influence of the structure, size, and composition of two-layered nanoparticles with a silver nanoshell situated in copper phthalocyanine films on the overall optical response of the hybrid nanomaterial was theoretically studied. The characteristics of surface plasmon resonance absorption (SPRA) bands and near-field scattering of the two-layered plasmonic nanospheres were investigated using Mie theory taking into account matrix absorption and internal size effects. It was shown that the SPRA band could be tuned to exciton absorption bands of the organic component by varying the refractive index and volume fraction of the dielectric core in nanoparticles with metal nanoshells. Two attenuation peaks with comparable intensities that were sensitive to a change of the system optical and geometric parameters were observed in a strong coupling regime in the visible spectral region. The results could be used to develop nanostructured functional elements for nanophotonics, photovoltaics, and sensing.

Keywords: *metal-containing two-layered nanoparticles, absorbing matrix, hybrid nanostructures, surface plasmon resonance absorption, near- and far-field scattering characteristics.*

Introduction. Plasmonic nanomaterials containing noble-metal nanoparticles (NPs) are famous for their unique and important properties associated with surface plasmonic resonance absorption (SPRA) in the visible spectral region and significant enhancement of local fields near the surface of the metallic NPs (hot spots) [1]. The leading developments in modern plasmonics and nanophotonics are being made on hybrid nanostructures with plasmonic NPs and nonmetallic active structural components and properties missing in the individual components included in the hybrid [2]. The creation of hybrid metal-semiconductor nanomaterials opened possibilities for simultaneous control of photon and electron distributions and changes over broad limits of both the optical and electrophysical properties of nanomaterials [3]. The functional features and unique properties of hybrid metal-semiconductor materials are interesting for solving problems in catalysis and photocatalysis, for developing hypersensitive and biological sensors, and for designing optical markers and multifunctional diagnostic nanoplatforms and hybrid nanoantennae [4–7]. Doping of plasmonic NPs increased the efficiency of the active elements for photovoltaics and improved the characteristics of polarizers based on organic films [8–10].

Near-field plasmon–electron/exciton (PE) couplings play an important role in forming the optical response of hybrid nanostructures containing plasmonic and semiconducting components [11]. Depending on the morphological characteristics of the nanocomposite, which affect the degree of spectral overlap of the SPRA bands of the metallic NPs and the absorption bands of the nonmetallic component, weak and strong PE-coupling can occur [12].

Various synthetic methods enabling the creation of hybrid nanomaterials of various morphologies, e.g., metal–shell structures with included metallic NPs and with metallic NPs on surfaces of thin semiconducting films, have been developed to produce hybrid structures containing plasmonic NPs and semiconductor structural elements [13, 14].

Hybrid nanocomposites with matrices of organic semiconductors into which two-layered NPs with a dielectric core and a metallic shell are incorporated are highly interesting. Absorption spectra of such two-layered NPs, which have been called nanoshells and feature two surfaces bordering the metal, are characterized by two spectrally resolved SPRA bands [15]. A study of nanoshells embedded in dielectric transparent matrices showed that the spectral positions and intensities of

*To whom correspondence should be addressed.

B. I. Stepanov Institute of Physics, National Academy of Sciences of Belarus, Minsk, Belarus; email: radynich@gmail.com. Translated from Zhurnal Prikladnoi Spektroskopii, Vol. 90, No. 5, pp. 728–737, September–October, 2023. Original article submitted May 22, 2023.

these SPRA bands could be effectively controlled by varying the refractive index of the dielectric core and the thickness of the metallic nanoshell [16].

The aim of the present work was to study features of the SPRA and near-field scattering characteristics of nanoshells embedded in matrices of organic semiconductors and to determine the potential for controlling the PE-coupling by targeted selection of the optic and geometric parameters of the nanoshells. Numerical simulation using extended Mie theory considering matrix absorption and internal size effects was performed for NPs with silver nanoshells embedded in copper phthalocyanine (CuPc).

Calculation Methods. Figure 1 shows a schematic illustration of hybrid NPs with a dielectric-core–metallic-shell structure. The center of the spherically symmetric NP coincides with the origin of a rectilinear Cartesian coordinate system. An incident planar monochromatic wave is polarized along the x axis ($\mathbf{E}_{\text{in}} \parallel 0x$) and propagates in the direction of the z axis ($\mathbf{k}_0 \parallel 0z$). Because the medium is absorbing, the amplitude of the electric field decreases as the wave propagates in it. The amplitude of the electric field in the $x0y$ plane is denoted E_0.

The spectral and near-field scattering characteristics of such two-layered plasmonic NPs embedded in absorbing organic semiconductor matrices were simulated using extended Mie theory [17–26]. The following expression was used for numerical calculations of extinction efficiency factor Q_{ext} [25, 26]:

$$Q_{\text{ext}} = \frac{4\kappa_m^2}{n_m\left[1+\mathrm{e}^{\hat{a}}(\beta-1)\right]}\,\mathrm{Re}\left\{\frac{1}{\kappa_m - in_m}\sum_{n=1}^{\infty}\left[(2n+1)\left(\psi_n^*\psi_n' - \psi_n\psi_n'^* + b_n\psi_n'^*\xi_n + b_n^*\psi_n\xi_n'^* - a_n\psi_n^*\xi_n' - a_n^*\psi_n'\xi_n^*\right)\right]\right\}, \quad (1)$$

where n_m and κ_m are the real and imaginary parts of the matrix complex refractive index; $\beta = 4\pi R_2\kappa_m/\lambda_0$, λ_0 is the incident radiation wavelength; R_1 and R_2, radius of core and outer radius of two-layered particle; a_n and b_n, Mie coefficients depending on the optical constants of the core (n_1 and κ_1), shell (n_2 and κ_2), and matrix and on the core and shell diffraction parameters $\rho_{1(2)} = 2\pi R_{1(2)}/\lambda$; ψ_n, ξ_n, ψ_n', ξ_n', Riccati–Bessel functions and their derivatives; h_n, spherical Hankel function of the first kind of order n; and *, denoting the complex conjugate.

Let us use the scattering efficiency factor in the near field Q_{NF} to estimate near-field effects [27]. It characterizes the intensity increase of the field on the surface of a sphere of radius R_s upon introducing NPs into the center of the sphere. The quantity Q_{NF} for a spherical NP situated in an absorbing medium is calculated based on classical formulas for the scattering characteristics of the near field [28] using the expression [26, 29]:

$$Q_{\text{NF}} = \frac{\left(4\pi\kappa_m R_s\right)^2}{\lambda_0^2\left[1+\mathrm{e}^{\beta}(\beta-1)\right]}\sum_{n=1}^{\infty}\left\{|a_n|^2\left[(n+1)|h_{n-1}|^2 + n|h_{n+1}|^2\right] + (2n+1)|b_n|^2|h_n|^2\right\}. \quad (2)$$

The optical constants of the metallic component in Eqs. (1) and (2) are dimensionally dependent for metal-containing NPs and nanoshells, the sizes of which are comparable to the electron mean free path in the corresponding bulk material. Effects associated with this are often called internal free-path effects [1, 30]. These effects for noble metals can be considered by approximating the limiting conductivity-electron mean free path (LCEMFP) [30]. The approximation consists essentially of assuming that the dielectric permittivity of the corresponding bulk metal obeys the Drude model whereas the collision of free electrons with the surface of the NP metal part becomes an additional source of energy loss for them. As a result, the size-dependent decay constant for a metal-containing NP is written:

$$\gamma_{\text{NP}} = \gamma_0 + v_{\text{F}}/L\,, \quad (3)$$

where γ_0 is the decay constant for the bulk sample; v_{F}, the Fermi velocity; L, the electron mean free path in the particle determined by collisions with the bordering metal surfaces. The quantity $L = R_{\text{NF}}$ with diffusion scattering of electrons on the surface of a spherical homogeneous metal NP. The additional energy losses of free electrons become increasingly greater as the NP size becomes increasingly smaller than the electron mean free path. The dielectric constant associated with the contribution of free electrons is determined by the expression:

$$\varepsilon_{\text{NP}}(\omega, R_{\text{NP}}) = 1 - \omega_{\text{p}}^2/(\omega^2 + i\gamma_{\text{NP}}\omega)\,,$$

where $= N_0e^2/m_e\varepsilon_0$; ω_{p}, the plasma frequency of the bulk metal; N_0, the density of free electrons; e and m_e, the electron charge and mass. The overall scheme for calculating the size-dependent dielectric constant in terms of ballistic theory in

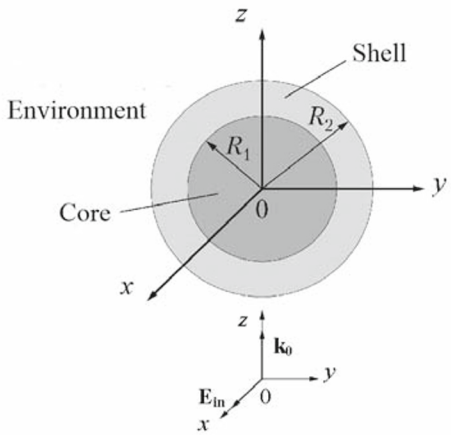

Fig. 1. Schematic illustration of a two-layered spherical particle.

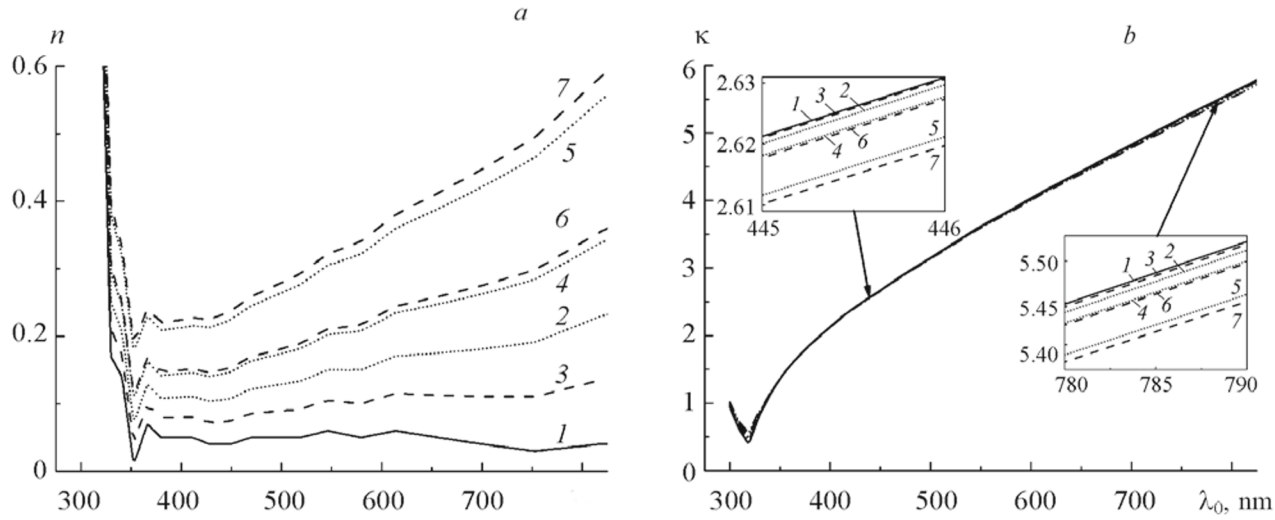

Fig. 2. Spectral dependences of refractive index (a) and absorption (b) of bulk silver (1), homogeneous spherical silver NPs of radius 10 (2) and 20 nm (3), and spherical silver nanoshells of thickness 5 (4, 6) and 3 nm (5, 7); external radius of metal-containing particles 10 (4, 5) and 20 nm (6, 7).

the LCEMFP approximation for homogeneous spherical NPs has been described [31]. This model was successfully used to calculate spectra of Q_{ext}, Q_{sca}, and Q_{abs} for spherical Ag, Au, and Cu NPs surrounded by a nonabsorbing medium [31–33]. The influence of internal size effects on SPRA characteristics and near-field scattering of spherical Ag NPs embedded in absorbing matrices was analyzed before [29].

A modification of the Kreibig model for metallic nanoshells deposited on a spherical core of another material was proposed [15] where the effective electron mean free path was:

$$L(R_2, a) = R_2\left[\frac{1}{1+a^2} - \frac{a}{2} - \frac{1}{4}\frac{1-a^2}{1+a^2}(1-a)\ln\frac{1-a}{1+a}\right]. \quad (4)$$

Here, $a = R_1/R_2$ and $0 < a < 1$. For $R_1 \to 0$, Eq. (4) converts into the expression $L = R_2$, which was obtained before for a homogeneous metal sphere [30].

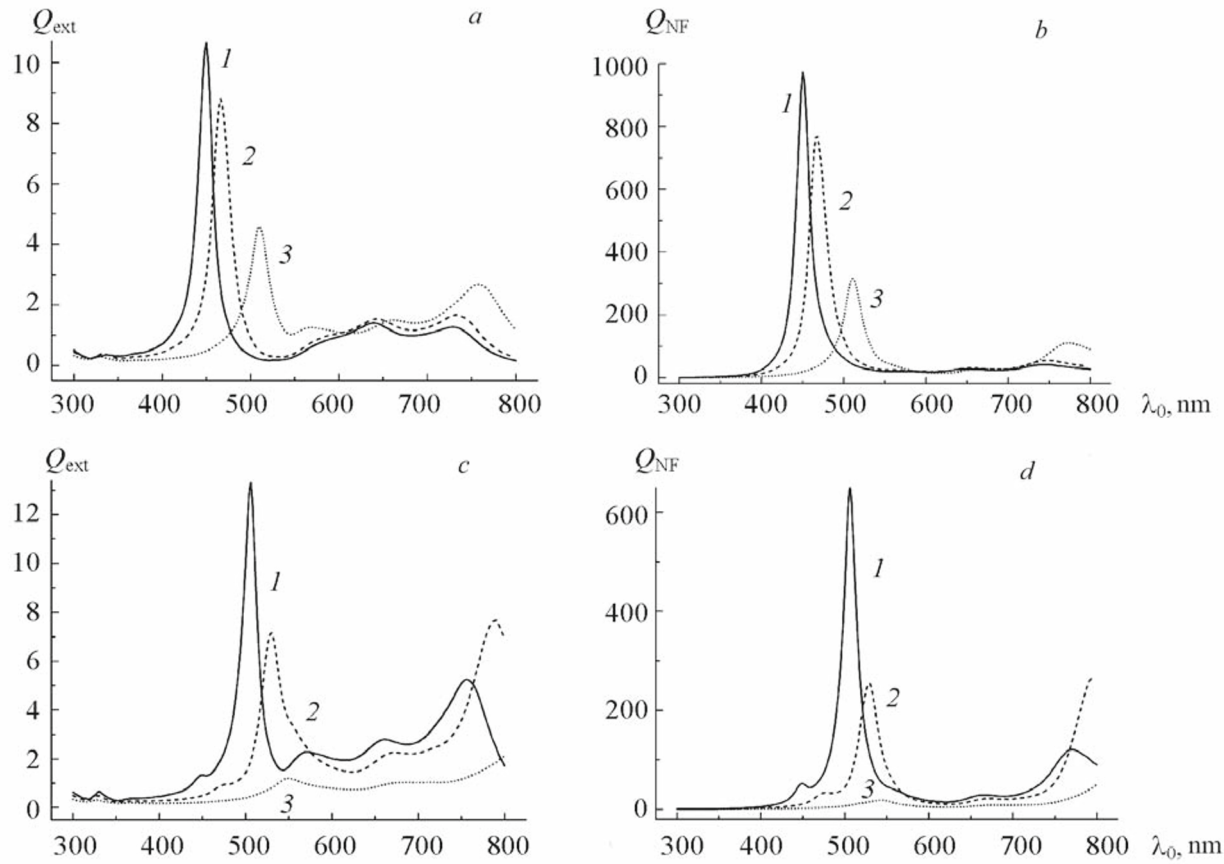

Fig. 3. Spectral dependences of extinction efficiency Q_{ext} (a, c) and near-field scattering Q_{NF} factors (b, d) of two-layered spherical particles with silver shells situated in CuPc; R_2 = 10 (a, b) and 20 nm (c, d); shell thickness 7 (1), 5 (2), and 3 nm (3); n_1 = 1.5.

The proposed model [15] for calculating internal size effects in a metal shell was successfully used to calculate the scattering and absorption characteristics of metal-containing nanoshells situated in nonabsorbing matrices [34, 35]. Figure 2 illustrates the application of this approach to silver nanoshells. The optical constants of bulk silver [36] and $\omega_p = 1.38 \cdot 10^{16}$ s^{-1}, $\gamma_0 = 2.73 \cdot 10^{13}$ s^{-1}, $v_F = 1.4 \cdot 10^6$ m/s [1, 28, 31] were used. Consideration of internal size effects for both solid silver nanospheres and silver nanoshells was shown to affect more strongly the real part of the complex refractive index of silver, causing it to decrease in the range 300–800 nm. Figure 2a shows that decreasing the radius of solid silver NPs from 20 to 10 nm doubled the deviation of the refractive index of a homogeneous silver nanosphere from that of bulk silver. The influence of internal size effects on the real part of the complex refractive index was even more significant for nanoshells, where additional energy losses of free electrons arose because of their collisions with the two nanoshell surfaces. In this instance, the contribution of internal size effects depended on both the thickness of the metal shell and its inner and outer radii. The imaginary part of the silver complex refractive index (Fig. 2b) depended insignificantly on the sizes of the solid nanospheres and the nanoshells.

Results and Discussion. Figure 3 shows results from numerical calculations of the spectral dependence of the extinction and near-field scattering efficiency for two-layered particles with silver shells embedded in CuPc. The CuPc absorption band maxima appeared near 340, 625, and 695 nm [37]. The SPRA band could be shifted in two ways, i.e., by a change of the external radius (R_2) of the two-layered particle due to a change of the size of the dielectric core (R_1) while holding the thickness of the plasmonic shell constant ($R_2 - R_1$) and by changes of the thickness of the plasmonic shell and the size of the dielectric core while holding the external radius of the two-layered particle constant. According to the literature [13, 38], a shift of the SPRA band relative to the CuPc absorption bands led to a change of the PE-coupling regime. A weak coupling regime of the plasmonic and organic components occurred where the CuPc absorption band and the SPRA

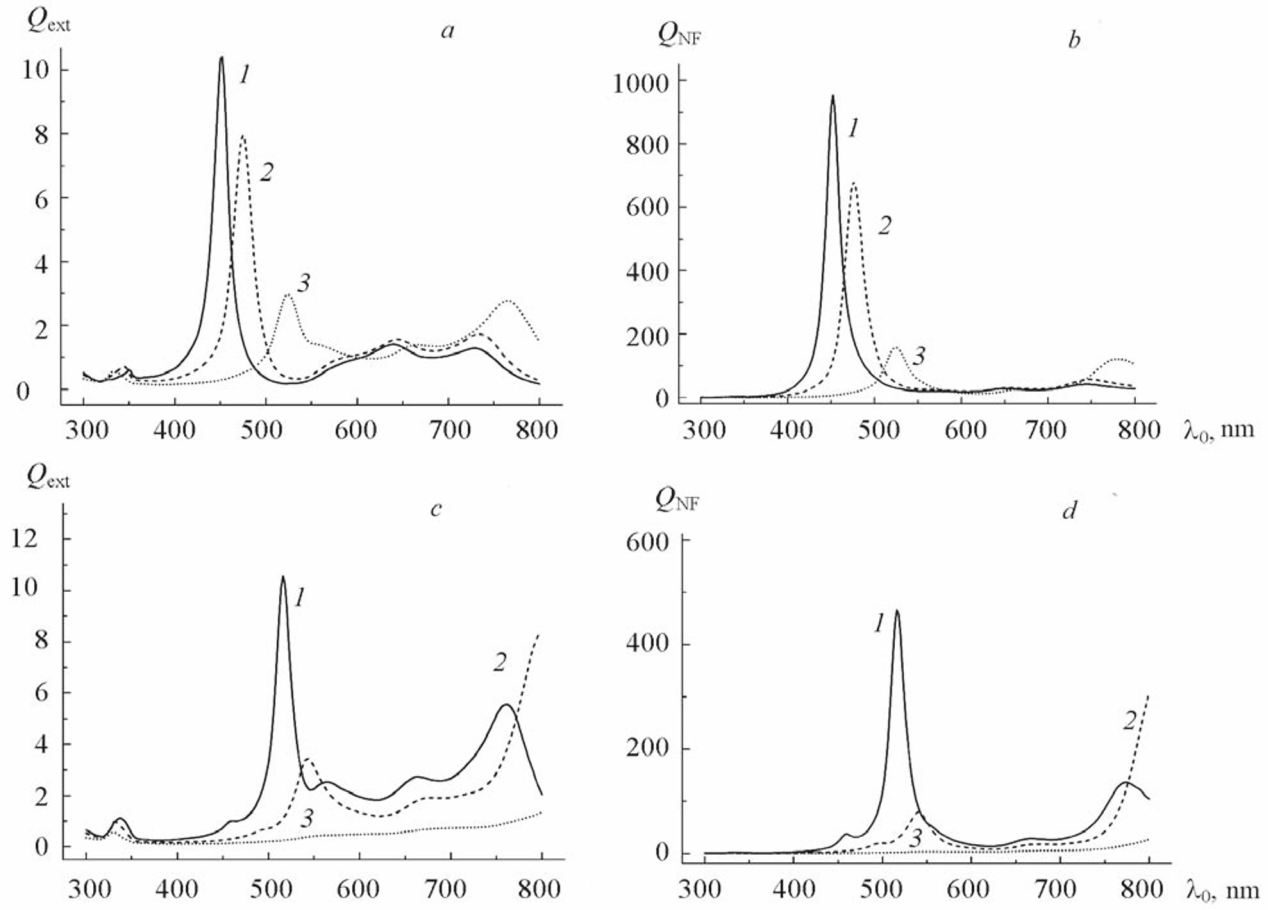

Fig. 4. Spectral dependences of extinction efficiency Q_{ext} (a, c) and near-field scattering Q_{NF} factors (b, d) of two-layered spherical particles with silver shells situated in CuPc; R_2 = 10 (a, b) and 20 nm (c, d); shell thickness 7 (1), 5 (2), and 3 nm (3); n_1 = 2.0.

band of the silver nanoshell were spectrally separated and/or the spectra slightly overlapped. This separation of the bands was achieved for small volume fractions of the dielectric core in the two-layered NP. Figure 3a and c (curve 1) show that a strong SPRA band was observed and Q_{ext} near the CuPc absorption bands (625 and 695 nm) increased in the extinction spectrum of the two-layered NPs with a silver shell in weak-coupling regime. The SPRA band was situated near 450 and 506 nm for R_2 = 10 and 20 nm. A long-wavelength shift and significant suppression of the SPRA band intensity occurred (Fig. 3a and c, curves 2 and 3) if the thickness of the silver shell was decreased.

Figure 3b and d shows the dependences of the near-field scattering efficiency factor Q_{NF} on the external size of the two-layered NP and the thickness of the plasmonic shell. One strong Q_{NF} band (curves 1) was observed for large thicknesses of the silver shell, where the volume fraction of the dielectric core was small. The maximum of this Q_{NF} band was close to the maximum of the corresponding SPRA band. The Q_{NF} band, like SPRA, shifted to longer wavelength (from 450 to 506 nm) and its intensity decreased (from 974 to 653) as the external size of the two-layered NP R_2 increased from 10 to 20 nm. Apparently, this was related to a decrease in the curvature of the external NP surface and the contribution of nonhomogeneous subsurface waves.

The spectral positions and intensities of the SPRA and Q_{NF} bands could be additionally adjusted by changing the dielectric characteristics of the core in two-layered NPs with a metal shell. Figure 4 shows the characteristics of the extinction and near-field scattering for two-layered NPs with silver shells embedded in CuPc with a core-material refractive index n_1 = 2.0. The qualitative trends in the influence of the metal-shell thickness on the spectral dependences of the extinction efficiency Q_{ext} and near-field scattering Q_{NF} of two-layered spherical NPs that were observed in Fig. 3 persisted upon increasing the refractive index of the core. In this instance, an increase in the thickness of the metal shell (keeping the

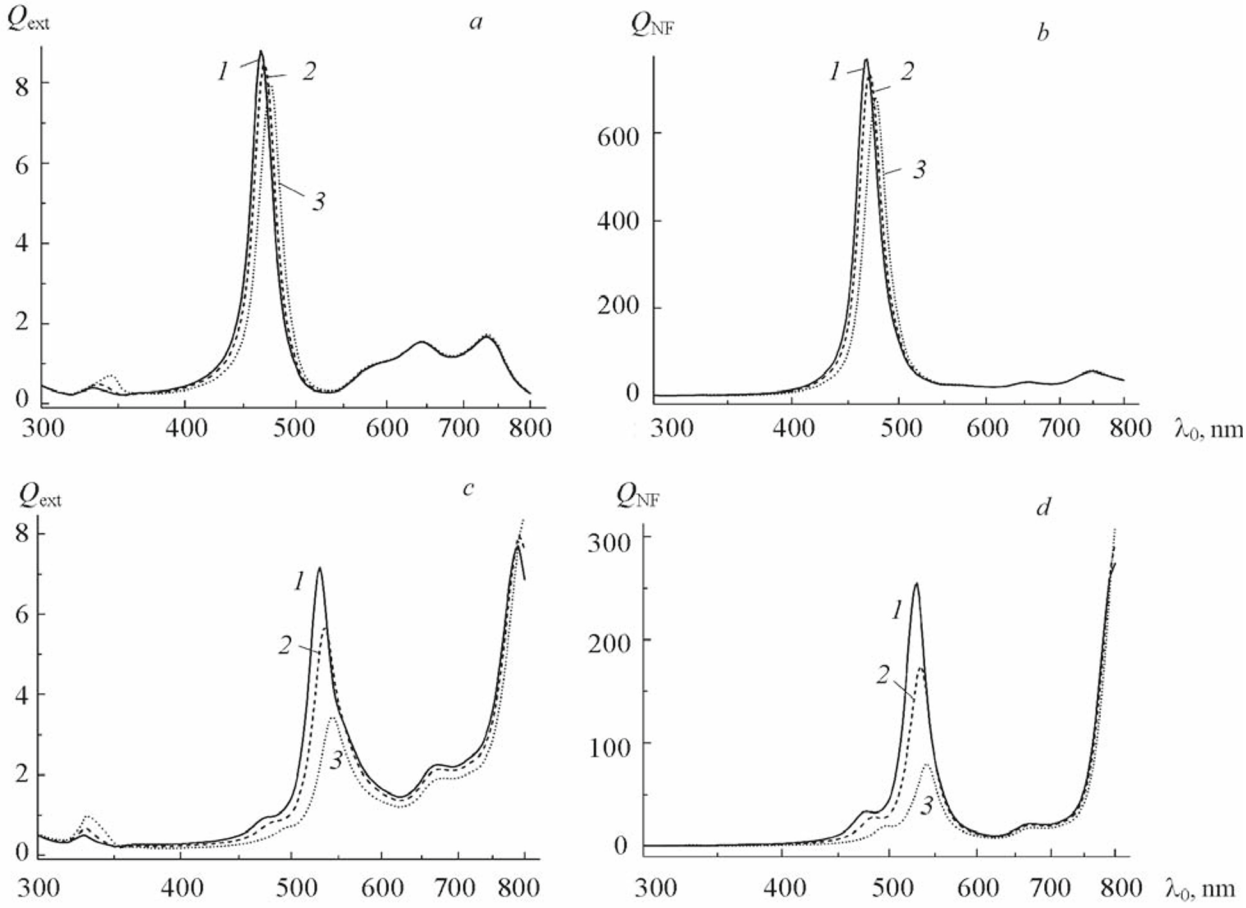

Fig. 5. Spectral dependences of extinction efficiency Q_{ext} (a, c) and near-field scattering Q_{NF} factors (b, d) of two-layered spherical particles with silver shells situated in CuPc; R_1 = 10 (a, b) and 20 nm (c, d); shell thickness 5 nm; n_1 = 1.5 (1), 1.7 (2), and 2.0 (3).

external NP size unchanged) also led to a short-wavelength shift and an increase in the maximum Q_{ext} and Q_{NF} values. A comparison of Figs. 3 and 4 showed that an increase in the core refractive index led to a decrease in the maximum Q_{ext} and Q_{NF} values although the sensitivity of the SPRA spectra to n_1 was more pronounced for intermediate values of the metal volume fraction in the two-layered NP.

Figure 5 shows the dependences of Q_{ext} and Q_{NF} for two-layered NPs with a constant external size (R_2 = 10 and 20 nm) and intermediate thickness of the silver shell (5 nm) that were embedded in CuPc on the change of core-material refractive index n_1 in the range 1.5–2.0.

Not only the degree of enhancement of near-field scattering but also the topology of the near-field distribution was important for practical applications. The topology of the near-field distribution and the dependences of the local field enhancement coefficients on the NP size and surrounding matrix properties were studied in detail for completely non-absorbing transparent matrices and homogeneous silver NPs [39]. It was found that the region of hot-spot concentration shifted to the forward hemisphere as the NP size increased. A nonmonotonic dependence of the maximum attainable local-field enhancement factor on the size of the silver nanospheres was observed. However, the presence of a dielectric core inside a metallic nanoshell and strong absorption of the matrix in which the two-layered NPs were embedded could affect the hot-spot intensity and the near-field distribution topology. Distributions of the internal and near fields for homogeneous silver NPs and NPs with a dielectric core and metallic shell were given to reveal this effect (Figs. 6 and 7). Figure 6 shows data for NPs embedded in CuPc. Calculations were performed for two regions, i.e., near the SPRA band (445 and 475 nm) and far from it (625 nm). A diminishing field propagated along the z axis and was polarized along the x axis. A color change from black to white meant that the field enhancement factor increased. Detuning of the SPRA band was

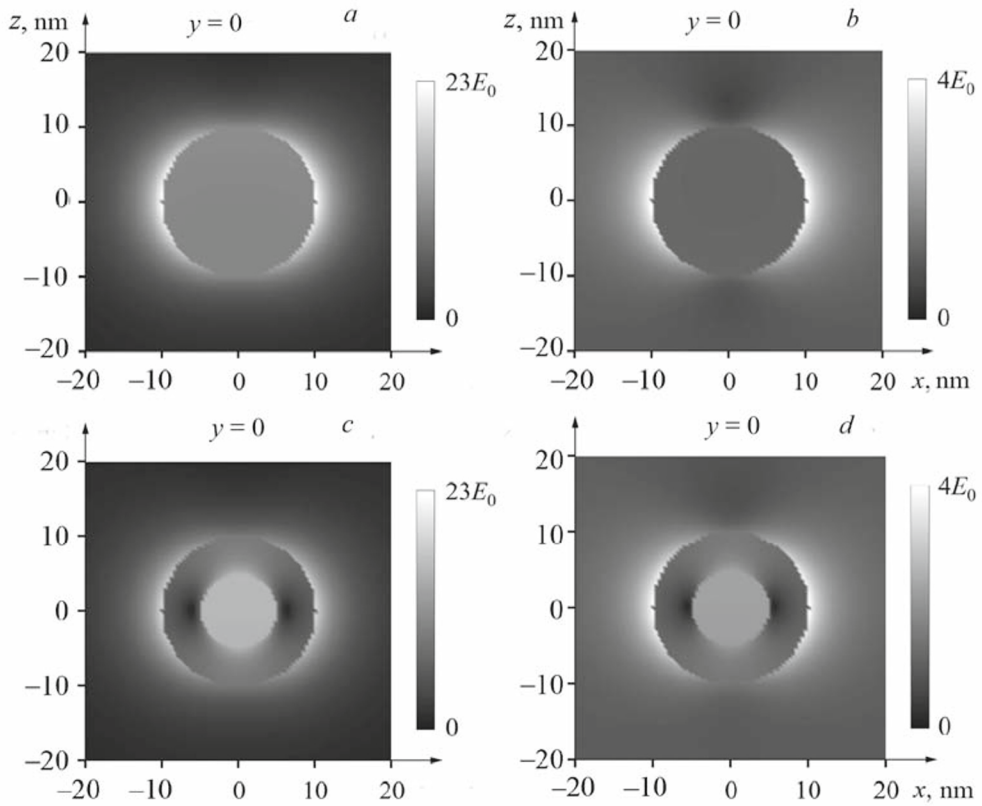

Fig. 6. Distribution of internal and near electrical fields of a homogeneous spherical silver NP of radius 10 nm (a, b) and a spherical NP with a dielectric core of radius 5 nm and a silver shell of thickness 5 nm (c, d); particles situated in CuPc; λ_0 = 445 (a), 475 (c), and 625 nm (b, d); n_1 = 2.0.

observed significantly to suppress the field enhancement effect near the NP surface. The maximum attainable near-field values near the SPRA band were $23E_0$ (for homogeneous silver NPs) and $19E_0$ (for two-layered NPs). Also, the maximum attainable near-field values at λ_0 = 625 nm practically did not exceed $4E_0$ for homogeneous and two-layered NPs. This was noted earlier for nonabsorbing matrices [39] and occurred in absorbing matrices for both homogeneous silver nanospheres (Fig. 6a and b) and two-layered NPs with a silver shell (Fig. 6c and d). The presence of a dielectric core inside a metallic shell was observed to redistribute internal fields in the spectral region near the SPRA bands and to concentrate regions of high fields inside the dielectric core. However, the electric field inside the metallic shell became highly nonuniform. For example, the field was $10–11E_0$ near the SPRA band inside a homogeneous silver particle (Fig. 6a) and $0–14E_0$ inside the silver shell itself (Fig. 6c). The field varied weakly inside the dielectric core, i.e., $15–16E_0$. It is noteworthy that cold regions in the silver shell neighboring hotter regions of the metallic shell and dielectric core were found.

Figure 7 shows calculated distributions of internal and near fields far from the SPRA band (at λ_0 = 695 nm) for NPs with a dielectric core and metallic shell embedded in a nonabsorbing matrix and in CuPc. The line contours join points with the same electric field strength. The difference in the field strengths between two neighboring contour lines is $0.23E_0$ (a), $0.24E_0$ (b), $0.27E_0$ (c), and $0.30\ E_0$ (d). The intensities of hot spots far from the SPRA band were observed to be comparable for both homogeneous silver NPs and two-layered NPs with a metallic shell that had the same volume. For example, $E_{max} = 4.27E_0$ for homogeneous silver NPs embedded in CuPc and $4.47E_0$ for nanoshells at λ_0 = 695 nm. However, the topologies of the near-field distribution patterns were sensitive to the NP structure. The asymmetry in the near-field distribution increased and the area occupied by the hottest spots expanded in the forward direction, being displaced into the shaded zone relative to the propagation direction of the incident radiation, upon going from homogeneous silver NPs to two-layered NPs. Comparisons of Fig. 7a and c in addition to Fig. 7b and d led to the conclusion that an increase in

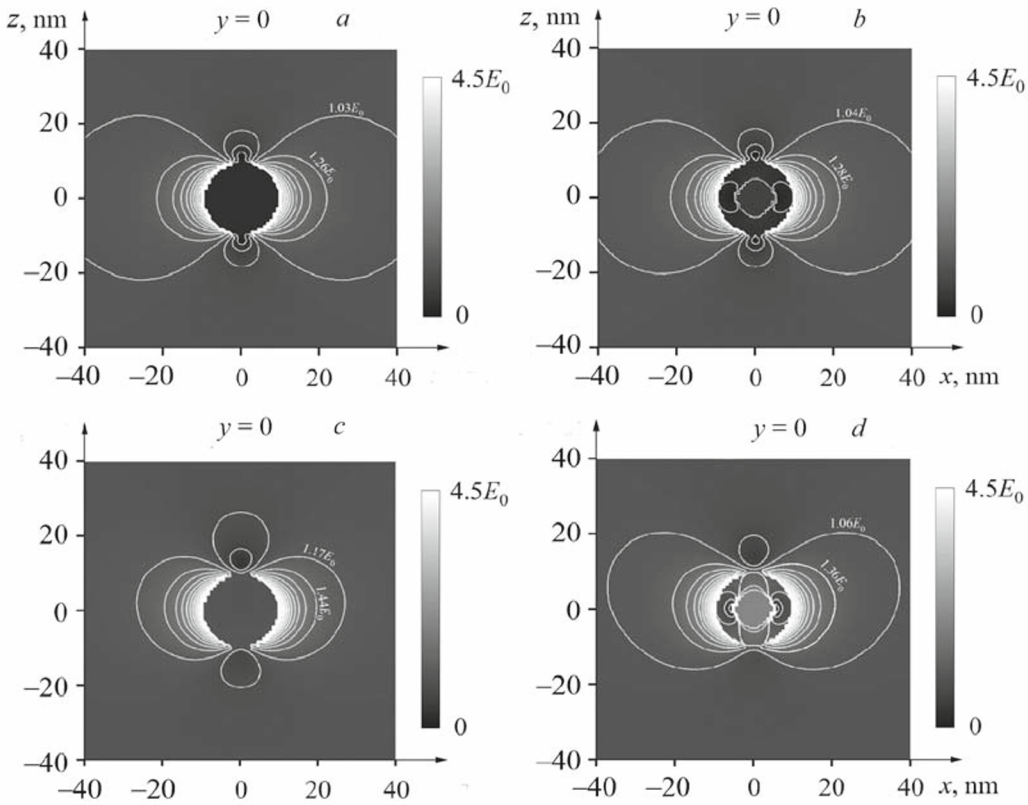

Fig. 7. Topology of distribution of electrical field for central cross section (y = 0) of a homogeneous spherical silver NP of radius 10 nm (a, c) and a spherical NP with a dielectric core of radius 5 nm and a silver shell of thickness 5 nm (b, d); NP situated in H_2O (a, b) and CuPc (c, d); λ_0 = 695 nm; n_1 = 2.0.

the matrix absorption not only increased the near-field decay rate with distance from the NP surface but also expanded the near-field distribution in the forward direction.

Figures 6 and 7 show that a dielectric field inside metal-containing NPs led to a substantial change in the distribution topology of the internal and near fields. The main feature consisted of hot spots near the SPRA band in metal particles with a dielectric core being much weaker than in fully metallic NPs. Nevertheless, a unique feature of two-layered NPs with a metallic nanoshell consisted of the ability to adjust the spectral position of the SPRA band relative to the absorption bands of selected nonmetallic components by varying the core optical and geometric parameters and the plasmonic shell thickness. It was of definite interest and could be used to control and tune the PE-coupling regime in hybrid nanostructures.

Conclusions. Numerical calculations were performed and the conditions for a targeted spectral shift of SPRA bands for two-layered NPs with a silver nanoshell embedded in a CuPc matrix were determined using extended Mie theory, which considers matrix absorption and internal size effects. It was shown that decreasing the thickness of the metallic shell (while keeping the NP external size and dielectric-core refractive index unchanged) led to a long-wavelength shift of the Q_{ext} and Q_{NF} maxima. This could be used to adjust the mutual spectral positions of extinction band maxima of plasmonic NPs and the organic matrix. The core refractive index had an insignificant effect on the spectral positions of the Q_{ext} and Q_{NF} maxima for the examined region of change of the geometric parameters of two-layered NPs. However, the Q_{ext} and Q_{NF} intensity maxima were highly sensitive to n_1 and appeared strongest for comparable volume fractions of metal and dielectric core. Two approximately equally intense spectral peaks that were sensitive to a change of the system optical and geometric parameters were observed in the visible region upon increasing the degree of overlap of the absorption bands of the organic component and the SPRA band in the strong-coupling regime. A transition from the weak-coupling regime to the strong-coupling regime was associated with a decrease of the field enhancement factor near the surface of two-layered NPs with

silver shells and faster extinction with distance from the NP surface. The results could be used to develop nanostructured functional elements for nanophotonics, photovoltaics, and sensing.

Acknowledgment. The work was supported in part by the Belarusian Republican Foundation for Fundamental Research (Grant No. F20EA-006).

REFERENCES

1. U. Kreibig and M. Volmer, *Optical Properties of Metal Clusters*, Springer, Berlin (1995).
2. S. I. Lepeshov, A. E. Krasnok, P. A. Belov, and A. E. Miroshnichenko, *Usp. Fiz. Nauk*, **188**, No. 11, 1137–1154 (2018).
3. J. Hicks, A. Tejeda, A. Taleb-Ibrahimi, M. S. Nevius, F. Wang, K. Shepperd, J. Palmer, F. Bertran, P. Le Fevre, J. Kunc, W. A. de Heer, C. Berger, and E. H. Conrad, *Nat. Phys.*, **9**, No. 1, 49–54 (2013).
4. S. Gurung, A. Singh, R. Chari, and J. Jayabalan, *J. Appl. Phys.*, **124**, No. 20, 204305 (2018).
5. V. K. Narasimhan, T. M. Hymel, R. A. Lai, and Yi Cui, *ACS Nano*, **9**, No. 11, 10590–10597 (2015),
6. R. Jiang, B. Li, C. Fang, and J. Wang, *Adv. Mater.*, **26**, No. 31, 5274–5309 (2014).
7. A. V. Povolotskaya, A. V. Povolotskii, and A. A. Man′shina, *Usp. Khim.*, **84**, No. 6, 579–600 (2015).
8. A. D. Pomogailo, A. S. Rozenberg, and I. E. Uflyand, *Metal Nanoparticles in Polymers* [in Russian], Khimiya, Moscow (2000).
9. A. D. Pomogailo, *Usp. Khim.*, **69**, No. 1, 60–89 (2000).
10. A. A. Toropov and T. V. Shubina, *Plasmonic Effects in Metal-Semiconductor Nanostructures*, Oxford University Press, Oxford (2015).
11. M. Haridas, L. N. Tripathi, and J. K. Basu, *Int. J. Nanosci.*, **10**, No. 04n05, 623–627 (2011).
12. F. Giazotto, F. Taddei, M. Governale, R. Fazio, and F. Beltram, *New J. Phys.*, **9**, 439 (2007).
13. V. S. Lebedev and A. S. Medvedev, *Kvantovaya Élektron. (Moscow)*, **42**, No. 8, 701–713 (2012).
14. G. A. Wurtz, P. R. Evans, W. Hendren, R. Atkinson, W. Dickson, R. J. Pollard, A. V. Zayats, W. Harrison, and C. Bower, *Nano Lett.*, **7**, No. 5, 1297–1303 (2007).
15. S. M. Kachan and A. N. Ponyavina, *J. Mol. Struct.*, **563**–**564**, 267–272 (2001).
16. G. P. Shevchenko, A. N. Ponyavina, S. M. Kachan, Z. M. Afanas′eva, and V. S. Gurin, *J. Appl. Spectrosc.*, **70**, 456–464 (2003).
17. M. Quinten and J. Rostalski, *Part. Part. Syst. Charact.*, **13**, 89–96 (1996).
18. A. N. Lebedev, M. Gartz, U. Kreibig, and O. Stenzel, *Eur. Phys. J. D*, **6**, 365–373 (1999).
19. Q. Fu and W. Sun, *Appl. Opt.*, **40**, No. 9, 1354–1361 (2001).
20. I. W. Sudiarta and P. Chylek, *J. Opt. Soc. Am. A*, **18**, No. 6, 1275–1278 (2001).
21. W. C. Mundy, J. A. Roux, and A. M. Smith, *J. Opt. Soc. Am.*, **64**, No. 12, 1593–1597 (1974).
22. P. Chylekt, *J. Opt. Soc. Am.*, **67**, No. 4, 561–563 (1977).
23. R. A. Dynich, *J. Opt. Soc. Am. A*, **28**, No. 2, 222–228 (2011).
24. M. I. Mishchenko, *Opt. Express*, **15**, No. 20, 13188–13202 (2007).
25. R. A. Dynich, A. N. Ponyavina, and V. V. Filippov, *J. Appl. Spectrosc.*, **76**, 705–710 (2009).
26. R. A. Dynich, A. N. Ponyavina, and V. V. Filippov, *Opt. Spektrosk.*, **110**, No. 6, 909–915 (2011).
27. B. J. Messinger, K. U. von Raben, R. K. Chang, and P. W. Barber, *Phys. Rev. B: Condens. Matter*, **24**, No. 2, 649–657 (1981).
28. C. F. Bohren and D. R. Huffman, *Absorption and Scattering of Light by Small Particles*, Wiley, New York (1983).
29. R. A. Dynich and A. N. Ponyavina, *Opt. Spektrosk.*, **130**, No. 11, 1681–1690 (2022).
30. U. Kreibig and C. V. Fragstein, *Z. Phys.*, **224**, 307–323 (1969).
31. S. M. Kachan and A. N. Ponyavina, *J. Phys.: Condens. Matter*, **14**, 103–111 (2002).
32. A. V. Uskov, I. E. Protsenko, N. A. Mortensen, and E. P. O'Reilly, *Plasmonics*, **9**, No. 1, 185–192 (2014).
33. A. D. Kondorskiy and V. S. Lebedev, *J. Russ. Laser Res.*, **42**, No. 6, 697–712 (2021).
34. T. V. Teperik, V. V. Popov, and F. J. Garcia de Abajo, *Phys. Rev. B: Condens. Matter Mater. Phys.*, **69**, Article ID 155402 (2004),
35. B. N. Khlobtsov, V. A. Bogatyrev, L. A. Dykman, and N. G. Khlebtsov, *Opt. Spektrosk.*, **102**, No. 2, 269–277 (2007).

36. P. B. Johnson and R. W. Christy, *Phys. Rev. B: Solid State*, **6**, No. 12, 4370–4379 (1972).
37. C. C. Leznoff and A. B. P. Lever, *Phthalocyanines: Properties and Applications*, VCH, New York (1996), Vol. 4.
38. A. N. Ponyavina, K. A. Barbarchuk, A. D. Zamkovets, and S. A. Tikhomirov, *Dokl. BGUIR*, **19**, No. 8, 15–19 (2021).
39. R. A. Dynich and A. N. Ponyavina, *J. Appl. Spectrosc.*, **75**, 832–838 (2008).